

Intracellular pressure controls the propagation of tension in crumpled cell membranes

Received: 17 July 2024

Accepted: 10 December 2024

Published online: 02 January 2025



Raviv Dharan^{1,2}, Avishai Barnoy^{2,3}, Andrey K. Tsaturyan^{2,3}, Alon Grossman^{1,2}, Shahar Goren^{1,2}, Inbar Yosibash^{1,2}, Dikla Nachmias⁴, Natalie Elia⁴, Raya Sorkin^{1,2}✉ & Michael M. Kozlov^{2,3}✉

Propagation of membrane tension mediates mechanical signal transduction along surfaces of live cells and sets the time scale of mechanical equilibration of cell membranes. Recent studies in several cell types and under different conditions revealed a strikingly wide variation range of the tension propagation speeds including extremely low ones. The latter suggests a possibility of long-living inhomogeneities of membrane tension crucially affecting mechano-sensitive membrane processes. Here, we propose, analyze theoretically, and support experimentally a mechanism of tension propagation in membranes crumpled by the contractile cortical cytoskeleton. The tension spreading is mediated by the membrane flow between the crumples. We predict the pace of the tension propagation to be controlled by the intracellular pressure and the degree of the membrane crumpling. We provide experimental support for the suggested mechanism by monitoring the rate of tension propagation in cells exposed to external media of different osmolarities.

Propagation of the elastic tension along cell membranes can mediate mechanical signal transduction along cell surfaces and the speed of this process sets the persistence time of temporary inhomogeneities of the in-plane membrane stresses. Therefore, the rate of membrane tension propagation has recently become one of the hot topics of Cell Mechanobiology^{1–5}.

The structural base of any biological membrane is a few nanometer-thick lipid bilayer that exhibits a 2D fluidity and an elastic resistance to deformations of bending and stretching-compression^{6,7}. Membrane tension^{6–8} is a stress emerging within the bilayer in response to the application to the membrane of stretching (leading to positive tensions) or compressing (leading to negative tensions) forces. The membrane tension is in many respects a 2D analogue of pressure in 3D fluids. Based on this analogy, a tension perturbation generated at some membrane location by local forces has been

expected to propagate along the whole membrane plane⁹ and serve as a mediator of cross-talks between mechanical events happening at different locations along the membrane^{9–11}. Specifically, the plasma membrane tension was proposed to coordinate such processes as cell movement and shape transformations^{9,12–16}, intracellular signaling^{17,18}, and axon growth and branching². Temporary inhomogeneities of membrane tension resulting from slow tension propagation can crucially affect local mechano-sensitive processes such as endo- and exocytosis^{19–22}.

Initially, the tension propagation in the membrane plane has been considered instantaneous compared to the biologically relevant time scales of seconds^{8,9,11,12,14,16,23–27}. The study of the propagation dynamics of tension perturbations in plasma membranes of live HeLa cells has challenged this notion¹. No measurable tension propagation was registered within about ten minutes between the regions of a plasma

¹School of Chemistry, Faculty of Exact Sciences, Tel Aviv University, Tel Aviv, Israel. ²Center for Physics and Chemistry of Living Systems, Tel Aviv University, Tel Aviv, Israel. ³Department of Physiology and Pharmacology, Faculty of Medical and Health Sciences, Tel Aviv University, Tel Aviv, Israel. ⁴National Institute for Biotechnology in the Negev (NIBN), Ben-Gurion University of the Negev, Beer Sheva 84105, Israel. ✉ e-mail: rsorkin@tauex.tau.ac.il; michk@tauex.tau.ac.il

membrane separated by 5–10 μm distances. Qualitatively similar results were obtained for numerous types of non-motile cells¹. At the same time, for the same cells a relatively fast spreading of tension, happening within a timescale of a few seconds, was observed within cell blebs¹, the spherical outgrowths of plasma membranes devoid of the sub-membrane layer of cortical cytoskeleton²⁸.

Yet, the following studies aiming to explore and verify the phenomenon of the ultra-slow spreading of tension perturbations in cell membranes resulted in a complex picture. The speed of the process varied over a few orders of magnitude wide range depending on the cell type, the region of the plasma membrane, and the way of the force application to the cell surface^{2–4}. In stark contrast to the results of *f*, in the goldfish retinal bipolar neurons, the tension perturbations were found to be rapidly transmitted within a few seconds to distances of 4 to 10 μm ³. This result was obtained for membranes of both the presynaptic terminals and the soma of these neurons. Testing in the same study the tension propagation in membranes of neuroendocrine chromaffin cells did not reveal any measurable tension transmission to the 6–12 μm distances within several minutes³, similar to the previous HeLa cell data¹. Conversely, large speeds of about 20 $\mu\text{m/s}$ were measured for the tension transmission in axons of rat hippocampal neurons². Yet, in contrast to the axons, no tension propagation within the relevant timescale was registered for the dendrites of the same cells², consistent again with the previous results¹. A relatively rapid propagation within several seconds to about 10 μm distances was observed for the membrane tension perturbations produced by activation of localized actin-driven membrane protrusions in the neutrophil-like cells⁴. Strikingly, tension perturbations generated by pulling a membrane tether within the same cells did not spread within several minutes to distances less than 2 μm ⁴. Summarizing, the rates of propagation of membrane tension perturbations measured in plasma membranes of diverse cells varied in the range between more than 10 $\mu\text{m/s}$ and less than 1 $\mu\text{m/min}$.

Understanding the physical mechanism behind the extreme slowness of the tension propagation in particular cell membranes, and, generally, wide variation range of the observed speeds of this process poses a challenge. Indeed, if a membrane was naively considered as a continuous and homogeneous elastic sheet suspended in an aqueous environment, tension perturbations would be expected to propagate with a speed of sound, which for lipid membranes was estimated to be in the range of 0.1–1.0 m/s²⁹ and, hence, exceeds by several orders of magnitude the highest measured rate of about 10 $\mu\text{m/s}$. Thus, the observed rates and, especially, the ultra-slow ones, must result from the membrane interactions with other cell structures. It has been suggested and experimentally substantiated that the slowing down of the tension spreading results from a mechanical cross-talk between the membrane and the underlying cortical cytoskeleton^{1–5}.

To put this hypothesis on a quantitative basis and relate it to the measurable material parameters of the lipid membranes, physical models were proposed in which the membrane was considered to be on average flat and coupled to the cortical layer by membrane-spanning anchor-proteins^{1,4,5}. The tension propagation was assumed to be mediated by the spreading of a perturbation of the in-plane lipid density that resulted from a local membrane stretching. To account for the observed rates of tension propagation, these models had to assume the membranes to be unrealistically soft for stretching.

Here we proposed, theoretically analyzed, and substantiated by experiments a different concept according to which the ultra-slow propagation of tension is inherently related to the membrane crumpling produced by the contraction of the cortical layer. In the suggested model, the tension in the membrane crumples is generated and maintained by the intracellular pressure and the compressing force applied to the membrane by the cortex. The propagation of tension perturbations is mediated by the membrane flow between the crumples and its rate is set by the interplay between the pressure value and the extent of the membrane crumpling.

Using the biologically plausible values of the system parameters, we predicted the experimentally observed low speeds of tension propagation for the characteristic intra-cellular pressures characterising, according to the literature, the cell interior of epithelial cells upon regular conditions.

We performed experiments supporting the model predictions by exploring the tension propagation in plasma membranes of live cells exposed to hypotonic external media.

Results

Model

We consider a non-stretchable fluid membrane containing a substantial amount of integral proteins, which span the membrane and are bound to the contractile cortical cytoskeleton^{30,31} that underlies the membrane cytoplasmic face^{1,32} (Fig. 1A). This membrane feature has been substantiated by observations of a transient immobilization in the membrane plane of a large fraction of abundant trans-membrane proteins and the dependence of this phenomenon on the cortical cytoskeleton^{1,32,33}. The mediators of the connection between trans-membrane proteins and the cortex include ezrin-radixin-moesin (ERM) proteins, merlin³⁴, myosin 1, and talin^{31,35}.

According to the picket-fence model^{32,36–38}, the trans-membrane proteins anchored to the cortex are organized in the membrane plane into a network of proteinic rows, which divide the membrane into compartments and represent barriers for the in-plane diffusion of the constituent membrane molecules^{39,40} and, hence, for the in-plane flow of the membrane material³³. While the compartments can vary in size, we assume them to be identical, for simplicity.

We consider the membrane within each compartment to bulge above the cortical layer (Fig. 1A), the latter representing the base plane of the system. We infer the intra-compartment membrane bulging to be caused by contraction of the cortical cytoskeleton, which results in the membrane buckling within each compartment and, hence, in the overall crumpled membrane conformation. This assumption is supported by the results on the interplay between the cortical contraction and the cell volume obtained for mitotic HeLa cells⁴¹. The cortex depolymerization removing the contraction resulted in an about 7%-increase in the cell volume⁴¹. Taking into account that this measurement was performed with blebbistatin-treated cells, while the blebbistatin activation results in about 5% volume decrease (see SI of⁴¹) the overall volume variation due to the contraction of the cortical cytoskeleton can be estimated to be about 12%. This cell volume variation is accompanied by the corresponding variation of the apparent membrane area which must be enabled by a reversible membrane crumpling.

The extent of the membrane crumpling will be quantified by the membrane excess area, β , defined as a relative difference between the membrane, A_m , and the base plane, A_b , areas of one compartment,

$$\beta = \frac{A_m - A_b}{A_b} \quad (1)$$

We consider the membrane to be subjected to an intracellular hydrostatic pressure, P ⁴², which originates from the trans-membrane osmotic gradients and can be controlled by changing the cell volume or the amount of the osmolytes^{41,43}. The intracellular pressure varies between a few tens Pa and a few thousand Pa depending on the cell type and the stage of the cell cycle⁴². Since the membrane is a continuous fluid elastic film, it sustains hydrostatic pressure. The cortical layer consisting of a network of actin-myosin fibers must be fully permeable to water and, therefore, does not sustain pressure.

Mechanism of tension propagation. The membrane within each compartment is exposed to two forces, the intracellular pressure, P (Fig. 1B), and a compressing force applied by the compartment

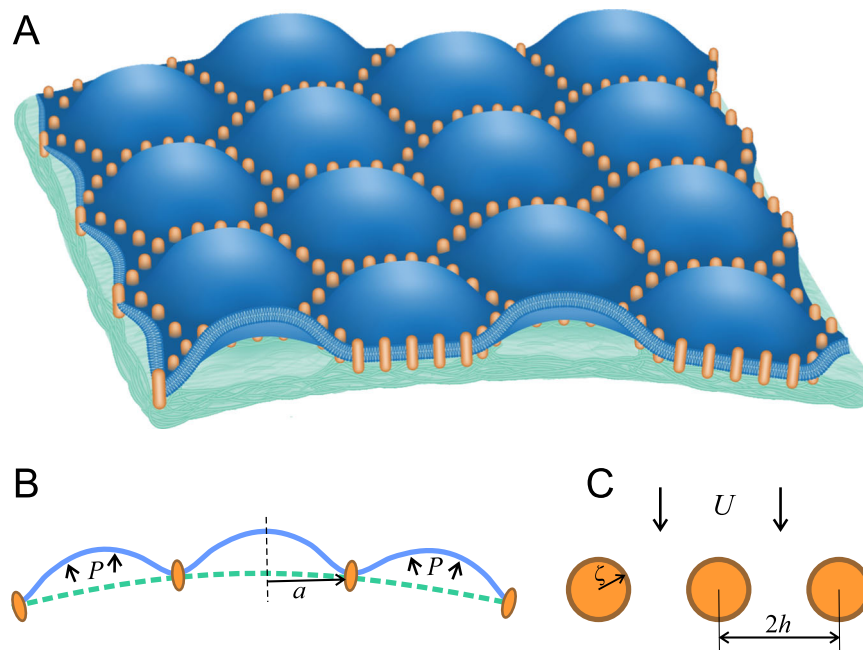


Fig. 1 | The illustration of the model and the notations. **A** The membrane is connected to the membrane skeleton by rows of transmembrane picket-proteins, according to the picket-fence model³². The protein rows subdivide the membrane into compartments and serve as barriers to the membrane flow. The membrane within each compartment bulges outwards because of a contraction of the membrane skeleton. **B** A schematic representation of the cross-sections of the dome-like

shapes of the membrane compartments and the notations. P is the intracellular pressure and a is the membrane compartment radius in the base plane. **C** A schematic representation of an element of the compartment boundary and the notations: ζ is the cross-sectional radius of a trans-membrane picket-protein, $2h$ is the center-to-center distance between two adjacent picket-proteins and U is the velocity of the 2D membrane flow.

boundary that drives the inter-compartment membrane bulging and, hence, determines the area excess, β . The interplay between these forces sets the membrane tension, γ . The relationship between γ , β , and P is derived in (SI A).

We start with an initial equilibrium state of the system in which the membrane tension is equal in all the compartments so that there is no membrane flow between the compartments. Keeping in mind that all the compartments are of the same size, and exposed to the same pressure, P , the tension homogeneity implies that the area excess, β , is equal for all the compartments (Eqs. A35, A36).

The equilibrium is perturbed by the extraction of some amount of the membrane area from one of the compartments, for example, by pulling out of it a membrane tether^{1,3,4}. The membrane bulge within the perturbed compartment becomes shallower and the compartment's area excess, β , decreases. As a result, the membrane tension within the compartment increases (see (Eq. A38)) and becomes larger than in the surrounding compartments.

The resulting disbalance of the tension induces a 2D membrane flow into the perturbed compartment through the compartment boundaries. This leads to a time-dependent redistribution throughout the system of the compartment area and to the related propagation of the tension perturbation.

The membrane flow rate and, hence, the speed of the tension propagation are determined by the values of the tension differences between the adjacent compartments, $\Delta\gamma$, and by the permeability of the compartment boundaries to the 2D lipid flow, λ (see SI B).

This propagation ceases when the membrane area and the tension are equalized again in all the compartments.

Model predictions

We theoretically analyzed the evolution in time and space of the membrane tension, γ , and the compartment excess area, β , following their perturbation in one membrane compartment. The mathematical derivations are presented in (SI C). The major result of the analysis is

that the perturbations propagate according to the diffusion-like relationship between the propagation distance, R , and time, t ,

$$t = \frac{R^2}{4D}, \quad (2)$$

with the effective diffusion coefficient, D , determining the propagation rate. The relationship between the diffusion coefficient and the system parameters is given by

$$D = 0.2 \frac{1}{\beta_0^{3/2}} \lambda a^2 P, \quad (3)$$

where β_0 is the unperturbed value of the compartment area excess, and a is the membrane compartment radius in the base plane. According to (Eq. 3), the tension propagation rate is predicted to increase with the intracellular pressure, P , the lipid permeability of the compartment boundary, λ , and the compartment size, a . The tension propagation is predicted to be slower for larger values of the initial area excess, β_0 . For nearly flat membranes with $\beta_0 \rightarrow 0$, the effective diffusion coefficient is predicted to be infinitely large even for small pressures. To account for a finite value of the diffusion coefficient in the limiting case of a flat membrane, the assumption of the non-stretchability of the membrane must be lifted.

To compare the quantitative predictions of the model with the previously reported observations, we use specific parameter values.

To evaluate the initial excess area, β_0 , we use the above-mentioned data⁴¹ on the increase of the cell volume resulting from the elimination of the cortex contraction. For rounded cells⁴¹, the nearly 12% large change in the volume corresponds to an increase in the apparent cell surface area of about 8%. Based on the latter number, we use for estimations the characteristic value of the membrane area excess generated by the cortex contraction to be $\beta_0 = 0.1$.

Because the typical radii of the membrane compartments vary in the range 30–230 nm^{32,44}, for the proof-of-principle estimations, we use a mid-value of $a = 100$ nm.

To estimate the 2D permeability of the proteinic boundaries of the membrane compartments (Fig. 1C) with respect to lipids, λ , we assume the in-plane cross-sectional radius of a trans-membrane anchor-protein, that comprises a stretch of hydrophobic amino acid residues structured as an α -helix⁴⁵, to be, $\zeta = 1$ nm, the half-distance between the adjacent anchor-proteins corresponding to boundary coverage by the proteins estimated in³⁶ to be, $h = 2.5$ nm, and the 2D membrane viscosity to have a value $\mu = 3 \cdot 10^{-9} \frac{\text{Ns}}{\text{m}}$. Using (Eq. B5) (see SI B) and⁴⁶ we obtain $\lambda \approx 0.05 \frac{\text{m}^2}{\text{Ns}}$. The intracellular pressure measured for different cell types varies in the range between a few tens Pa to several kPa⁴².

For cells with low internal pressures, such as $P = 40$ Pa measured during the interphase of HeLa cells⁴³, we estimate the diffusion coefficient, D , to be equal $D \approx 0.04 \frac{\mu\text{m}^2}{\text{s}}$, and the time of tension propagation (Eq. 2) to the experimentally relevant distance of $R = 10 \mu\text{m}$ to have a value of about $t = 10$ min, which agrees with the ultra-slow propagation of the membrane tension perturbations, as observed in¹ and in the dual-tether pulling experiments of⁴.

A propagation time, t , of a few seconds, as observed in the goldfish retinal bipolar neuron presynaptic terminals³ and hippocampal neurons² and by using a local optogenetic stimulation of the actin polymerization in neutrophil-like HL-60 cells⁴ can be easily explained by larger intracellular pressure, P . Specifically, the propagation time, $t \approx 1$ s, for the distance, $R = 3 \mu\text{m}$, requires the effective diffusion coefficient to be $D \approx 10 \frac{\mu\text{m}^2}{\text{s}}$. According to (Eq. 3) and the above-mentioned values of the parameters λ and a , the needed intracellular pressure is $P \approx 3 \text{ kPa}$. Assuming this pressure to be generated by a transmembrane osmotic difference, ΔC , and using the common relationship, $P = RT\Delta C$ (where RT is the product of the universal gas constant and the absolute temperature), we obtain that the required ΔC has a modest value of about 1 mM.

Importantly, the higher rates of propagation may result also from larger values of the compartment size, a , and of the permeability of the compartment boundaries, λ , and from smaller values of the initial excess area, β_0 (Eq. 3). However, realistic variations of a and λ cannot exceed a few folds and cannot, therefore, explain the few orders of magnitude wide range of variation of the effective diffusion coefficient, D . Thus, the pressure, P , and the excess area, β_0 , appear to be responsible for the observed differences in the rate of tension propagation. The predicted dependence of the effective diffusion coefficient, D , on β_0 and P is illustrated in (Fig. 2).

Experimental support for the model

Our goal here was to obtain experimental support for the control of the rate of membrane propagation by intracellular pressure, as proposed by our model. To alter the intracellular pressure, we used variations of the osmotic difference between the intra- and extracellular mediums.

Effects of hypotonic mediums on the rate of tension propagation.

First, we verified that the intracellular pressure affects the plasma membrane tension. HEK293T cells were stained with DiI-C12 (see Methods). Then the cells were incubated with HEPES buffer with a certain NaCl concentration (see Methods) and placed in the experimental chamber within the C-trap instrument, which combined dual trap optical tweezers and confocal fluorescence microscopy. Using an optically trapped bead, we pulled a tether from cells and measured the tether-pulling force, which is directly related to the plasma membrane tension in the vicinity of the tether origin⁴⁷. The experiment was performed for NaCl concentrations equal to or lower than the expected intra-cellular osmolarity of 150 mM. The rationale for this experiment is based on the previous work^{48,49} demonstrating that placing cells in a hypotonic medium increases the intracellular pressure, P , and the

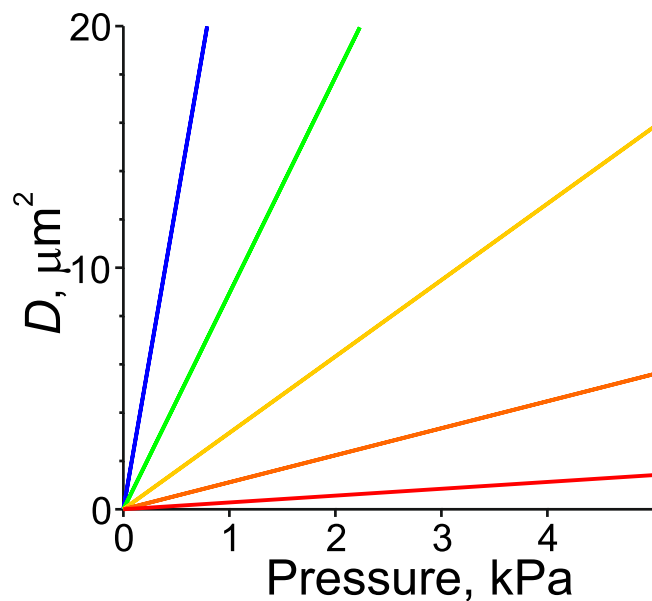


Fig. 2 | Tension diffusion coefficient. The dependence of the diffusion coefficient, D , on the initial excess area, β_0 , and intracellular pressure, P , for the parameter values: $\zeta = 1$ nm, $h = 2.5$ nm, $\mu = 3 \cdot 10^{-9} \text{ N s/m}$, $a = 100$ nm. The values of β_0 are indicated by the line color: red 0.5, orange 0.2, yellow 0.1, green 0.05, blue 0.025.

membrane tension, γ . The tether-pulling force of cells incubated in hypotonic solution, i.e., HEPES buffer with 50 mM NaCl, was significantly higher than that of cells incubated in isotonic solution, i.e., HEPES buffer with 150 mM NaCl (Supplementary Fig. D1), demonstrating the direct effect of changes of the extracellular osmolarity on membrane tension. For our measurements, we selected only tethers that appeared single in our confocal images. Yet we cannot exclude that some of them might have been double or even multiple tethers. This, probably, contributed, along with the variability between cells, to the spread of the measured values of the tether-pulling force (Supplementary Fig. D1).

We verified that in our system the rise in the intracellular pressure and membrane tension in hypotonic solution was not a transient effect that cells compensated for within a few seconds, as demonstrated in⁵⁰. Since the rise and recovery of tension and pressure in hypotonic conditions were coupled to the corresponding changes in the cell volume⁵⁰, we measured the volume dynamics of HEK293T cells in HEPES buffers with 50 mM and 150 mM NaCl. Cells that were incubated in 50 mM NaCl for 15 minutes were significantly larger than those in the isotonic solution (Supplementary Fig. D2 A-C). The volume of the cells remained relatively high even after 50 minutes (Supplementary Fig. D2 D) meaning that in our system no recovery of the cell volume occurred and, hence, the intracellular pressure and the related membrane tension remained constant within the time of our experiments.

Next, we tested the prediction of our model (Eq. 3), according to which an increase in the intracellular pressure, P , is expected to result in larger values of the effective diffusion coefficient, D , and, hence, to accelerate the tension propagation. For this purpose, we set up the orthogonal dual-tether pulling assay, which is a slightly modified version of the assay established in⁴. Two mutually perpendicular tethers were pulled out of the cell membrane using two optically trapped beads (Fig. 3A). Below we refer to the two beads and the corresponding tethers as bead 1, tether 1 and bead 2, tether 2 (Fig. 3A). We shifted bead 1 along the tether's axis, hence, changing the length of the tether 1 (Fig. 3B and Supplementary Movie 1) and monitored the response of the bead 2. The elongation of tether 1 was expected to locally perturb the membrane tension in the vicinity of the tether's origin. Propagation of this perturbation along the membrane till the origin of the tether 2

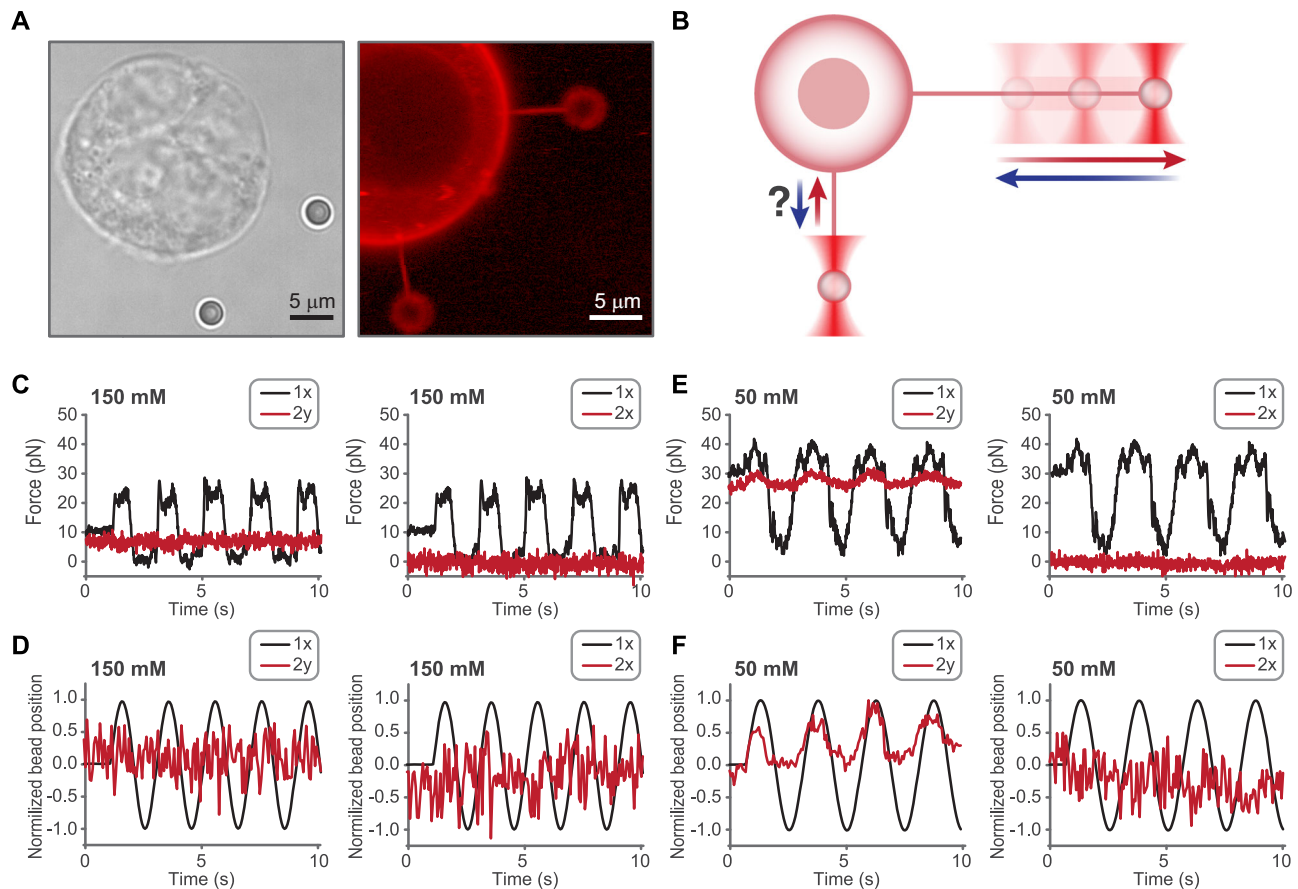


Fig. 3 | Orthogonal dual-tether pulling assay to monitor tension propagation in cells. **A** Bright-field microscopy (left) and confocal fluorescence microscopy (right) images of two orthogonal tethers pulled by two optically trapped beads from a HEK293T cell dyed with DiI-C12. **B** Schematic illustration of the orthogonal dual-tether assay to monitor membrane tension propagation. Bead 1 moves outwards the cell extending tether 1 and thereby increasing the local membrane tension. If the tension perturbation propagates along the cell membrane within the experimental timescale, bead 2 will start moving towards the cell in the direction perpendicular to that of bead 1. **C, D** Representative plots of the tether force (**C**) and the bead position (**D**) of the orthogonal dual-tether pulling assay conducted in HEPES buffer with 150 mM NaCl. The position of each bead was normalized to its

movement amplitude. Within the experimental accuracy, bead 2 did not respond to the movement of bead 1. $N = 19$ cells from 4 independent experiments. **E, F** Representative plots of the tether force (**E**) and the bead position (**F**) of the orthogonal dual-tether pulling assay conducted in HEPES buffer with 50 mM NaCl. The position of each bead was normalized to its movement amplitude. The left panels in (Fig. 3 C–F) correspond to the monitoring of the response of bead 2 in the direction perpendicular to that of the movement of bead 1. The right panels correspond to monitoring of the response of bead 2 in the same direction as that of the movement of bead 1. Note that the response of the bead 2 at 50 mM was only in the direction perpendicular to that of the movement of the bead 1. $N = 7$ cells from 3 independent experiments. Source data are provided as a Source Data file.

was anticipated to induce a shift of the bead 2 from its initial position. Specifically, considering the tether-pulling orientations shown in (Fig. 3A, B), moving bead 1 outwards the cell (to the right) was expected to cause bead 2 to move towards the cell (upwards). The time delay between the shift of bead 1 and the beginning of the movement of bead 2 was considered a measure of the time of the tension propagation between the origins of the two tethers. In practice, we oscillated the bead 1, recorded the induced oscillations of the bead 2 and used the time shift between the two oscillations to evaluate the rate of the tension propagation.

To test the predicted dependence of the tension propagation rate on the intracellular pressure P (Eq. 3), we started with experiments in isotonic conditions upon cell exposure to HEPES buffer with 150 mM NaCl. We did not observe within the experimental time scale of up to 6.75 minutes any response of bead 2 to the movement of bead 1 (Fig. 3C, D left panels, and Supplementary Fig. D3 and Fig. 4A). To confirm that shifting bead 1 indeed perturbed the local tension in the vicinity of the origin of tether 1, we measured the pulling force acting on this bead^{20,47}. This pulling force rose during the extension of tether 1 by moving bead 1 away from the cell, which evidenced the tension

increase. The pulling force in tether 1 dropped to zero when the tether was loosened by moving the bead 1 towards the cell. In summary, in isotonic conditions, the tension propagation was extremely slow, so the tension perturbations did not reach tether 2 within the time of the experiment.

Next, we incubated the cells in HEPES buffer with 50 mM NaCl corresponding to a hypotonic condition. We detected a response of the positions of bead 2 to the movement of bead 1 (Fig. 3E, F and Supplementary Fig. D4). The response of bead 2 was registered by measuring the pulling force acting on bead 2 and by using the subpixel resolution particle tracking analysis of the video recorded in the brightfield camera. The rise of the pulling force indicated that bead 2 was pulled towards the cell (Fig. 3E) as additionally verified by tracking the bead 2 position (Fig. 3F).

The response of the bead 2 looked instantaneous within the millisecond time-scale resolution of our experiments. Hence in the hypotonic medium the speed of the tension propagation was larger than a few microns per second. This value of the tension propagation rate is similar to those observed in^{2–4} for certain cells and conditions.

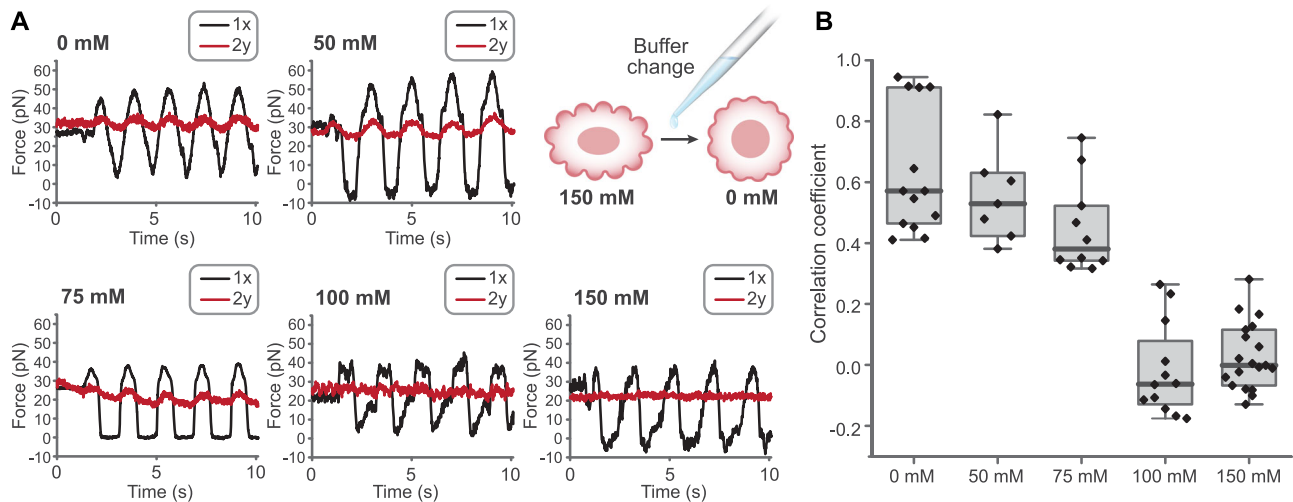


Fig. 4 | Transmembrane osmotic difference influences the membrane tension propagation. **A** The force-time plots obtained by the orthogonal dual-tether pulling assay conducted in HEPES buffer with different NaCl concentrations, as indicated. The measurements correspond to monitoring the response of bead 2 in the direction perpendicular to that of the movement of bead 1. **B** Box plot of

Pearson correlation coefficient between the movements of the two beads. From left to right: $N = 13, 7, 10, 12$ and 19 cells from 2, 3, 2, 3 and 4 independent experiments. Box-whisker plot horizontal lines represent (from the bottom) the 5%, 25%, 50%, 75%, and 95% of the data. Source data are provided as a Source Data file.

Importantly, the direction of movement of bead 2 was strictly along the axis of the tether 2 with no component in the direction of movement of bead 1. Since the two tethers were mutually orthogonal (Fig. 3 A, B, and Supplementary Fig. D4), the response of bead 2 was not related to the possible change of position of the whole cell, which could be induced by shifting bead 1. The response must result solely from the cross-talk between the two tethers mediated by the membrane tension propagation.

In addition to the above measurements, we probed the same type of experiments but with a system configuration like that of the previous studies¹ where the two tethers were pulled in nearly the same direction and were, therefore, approximately parallel (Supplementary Fig. D5 A). In most experiments of this type, bead 2 moved in the same direction as bead 1, suggesting that the contribution of the whole cell movement to the response of bead 2 might be significant for the parallel tether configuration. Nevertheless, even in this configuration, we were occasionally able to detect the response movement of bead 2 in the direction opposite to that of bead 1 (Supplementary Fig. D5 B).

To further verify the effect of the transmembrane osmotic difference on the propagation of the membrane tension, we conducted experiments in HEPES buffers with additional NaCl concentrations. We observed a significant response of the bead 2 position to the bead 1 movement for the NaCl concentrations of 0, 50 and 75 mM (Fig. 4A). For the NaCl concentrations of 100 mM or higher we did not detect any response of bead 2 within the experimental time scale of up to 6.75 minutes (Fig. 4A).

To quantify the correlation between the movements of bead 1 and bead 2, we calculated the Pearson correlation coefficient between the signals corresponding to the movements of the two tethers (Fig. 4B). Correlations between either the tether forces or the bead positions were calculated and jointly displayed. The analysis demonstrated a strong correlation between the movements of the two beads for the NaCl concentrations of the buffer of 0–75 mM, whereas for 100 and 150 mM NaCl concentrations there was no significant correlation.

Note that the amplitude of force variations applied to bead 2 was always substantially smaller than that applied to bead 1. This reflects the decay of the tension perturbation with distance as predicted by the diffusion-like model of tension propagation introduced in the previous section. The supplementary (Fig. D6) provides a quantitative characterization of this decay.

Possible indirect effect of hypotonic mediums on the rate of tension propagation. Besides altering the intracellular pressure, the exposure of cells to hypotonic mediums could affect the structure and stability of the cortical cytoskeleton, and, hence, indirectly influence the cytoskeleton-related compartmentalization of the plasma membrane by the proteinic fences through changes of the average membrane compartment size, a . In addition, the permeability of the compartment boundaries, λ , could be affected through changes of the density of the cytoskeleton-associated trans-membrane proteins constituting the fences. Both a and λ are predicted to influence the effective diffusion coefficient, D , determining the rate of tension propagation (Eq. 2).

Specifically, the hypotonic mediums could promote the detachment of the cortical cytoskeleton from the membrane accompanying the cell swelling. This would partially or fully dissociate the boundaries between the membrane compartments formed by rows of the anchor-proteins connecting the membrane to the underlying cortical cytoskeleton. This would increase both, a and λ , hence increasing the effective diffusion coefficient, D . A complete dissociation of these boundaries would render the rate of tension propagation as large as in the cell blebs.

To test the potential alterations of the membrane compartmentalization by the hypotonic mediums we first performed a sliding tether assay (Fig. 5). In this assay, we pulled a tether out of a cell membrane using an optically trapped bead. Then we attempted to drag the origin of the tether along the membrane plane by moving the bead sideways. If the boundaries of the membrane compartments were intact, they would restrict the movement of the tether's origin. If the compartment boundaries dissociated, the tether origin would slide along the membrane plane similar to our observations in bleb-like giant plasma membrane vesicles (GPMVs) (Fig. 5 and Supplementary Movie 2)⁵¹.

First, we performed this assay under isotonic conditions to confirm that the tether's origin is indeed confined. The results showed that in HEPES buffer with 150 mM NaCl, the origin of the tether did not slide upon moving the bead sideways (Fig. 5 and Supplementary Movie 3). Then we did the experiments in the hypotonic solution of HEPES buffer with 50 mM NaCl. Also in these conditions, the tether's origin was confined, indicating that the compartment boundaries remained intact. However, in a more hypotonic solution, e.g. HEPES buffer with

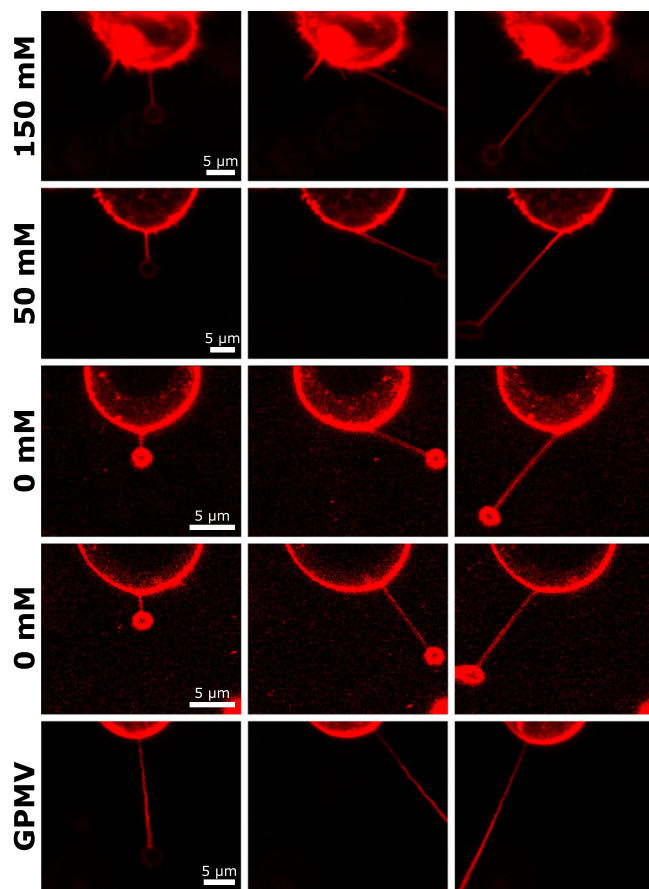


Fig. 5 | Sliding tether assay. HEK293T cells were dyed with DiI-C12 and incubated in HEPES buffer with different NaCl concentrations, as indicated. Next, a membrane tether was pulled out of the cell and then the bead was moved sidewise. Data was acquired from 3 independent experiments. At 50 and 150 mM NaCl, the tether origin did not slide along the cell plane in spite of the bead movement (20 and 17 cells for 50 mM and 150 mM, respectively). At 0 mM NaCl in 4 out of 10 cells, the tether origin did not slide significantly, while in the remaining cells or in the experiments conducted on 3 GPMVs, the tether origin freely slid.

no NaCl some tether origins were confined while others freely moved (Fig. 5 and Supplementary Movie 4).

Further, the dissociation of the inter-compartment boundaries must increase the rate of the in-plane diffusion of the membrane components to distances exceeding the typical compartment size³². To rule out this effect, we performed fluorescence recovery after photobleaching (FRAP) experiments to examine lipid diffusion at different osmolarities (Supplementary Fig. D7). The results showed that the lipid diffusion did not change significantly upon variation of NaCl concentration in the outside solution in the range between 0–150 mM (Supplementary Fig. D7 C). As a control, we conducted FRAP experiments on GPMVs, where the lipid diffusion rate was significantly higher than that measured in cells exposed to hypotonic media.

Finally, we addressed the possible changes in the compartment size by the single protein diffusion assay. We measured the time dependence of the MSD (mean square displacement) of EGFR in HEK293T cells incubated in HEPES buffer with 0, 50 and 150 mM NaCl (Supplementary Fig. D8). The underlying idea of these experiments was that the compartment boundaries consisting of immobilized membrane-spanning proteins must affect, in addition to the long-range diffusion, also the short-range diffusion of mobile membrane proteins. The latter effect is expected to be driven by the interaction between the mobile and immobilized membrane proteins mediated by the in-plane membrane flows⁵². For smaller compartment sizes lower

effective diffusion coefficients and, hence smaller slopes of MSD as a function of time must be expected.

Our results show (Supplementary Fig. D8) that short-range diffusion of the mobile protein in cells exposed to 50 mM and 150 mM NaCl solutions was greatly slowed down compared to that in cells incubated in 0 mM NaCl solutions (Supplementary Fig. D8). At lag time $t = 1$ s, the median MSD measured in 50 mM and 150 mM NaCl was, respectively, $0.0086 \pm 2.7 \cdot 10^{-4} \mu\text{m}^2$, and $0.0083 \pm 3.1 \cdot 10^{-4} \mu\text{m}^2$, while for 0 mM NaCl we measured the MSD of $0.1459 \pm 6.50 \cdot 10^{-3} \mu\text{m}^2$ (errors given are standard errors). Since, as mentioned above, the compartment size must restrict the short-range protein diffusion, these data support the assumption that the compartment boundaries did not significantly change within the osmolarity range of 50 to 150 mM NaCl. In comparison, a strong cell swelling in solution with 0 mM NaCl resulted in a drastic acceleration of the protein diffusion which must result from a substantial distortion of the compartment boundaries.

Discussion

The propagation rate of membrane tension perturbations is a recently emerged and controversial topic in cell biophysics. Initially, local variations of membrane tension have been assumed to spread instantaneously over cell plasma membranes, hence, serving as efficient transducers of mechanical signals along cell surfaces and preventing long-living inhomogeneities of membrane tension. Yet, recent experiments revealed a strikingly large variation range of the tension propagation rates, which encompassed, depending on the cell type and the cell region, very slow speeds of less than $1 \mu\text{m}/\text{min}$ and relatively large ones exceeding $10 \mu\text{m}/\text{s}$ ^{1–4}. The physical mechanisms accounting for these observations have remained debatable.

The previous models of this phenomenon assumed that the tension propagation is mediated by spreading in the membrane plane of a local distortion of the in-plane density of the membrane material i.e. a local area stretching induced by a local tension perturbation. The friction forces slowing the propagation were considered to build up between the membrane and the immobile anchor-proteins randomly distributed in the membrane plane, spanning the membrane matrix and connecting it to the layer of cortical cytoskeleton^{1,4,5}. The energy dissipation by these forces and, thus, the limitation of the propagation speed, were proportional in this model to the degree of the membrane stretching by the imposed tension. The larger the stretching, the more intensive the energy dissipation and the slower the tension propagation. Hence, the tension propagation speed was predicted to be proportional to the membrane stretching modulus^{1,4,5}.

While these models offered a qualitative explanation of the slowing down the membrane tension propagation, their ability to quantitatively account for the observed values of the propagation speed remained questionable. Indeed, the established values of the membrane stretching modulus are of the order of $10^5 \text{ pN}/\mu\text{m}$ ⁷. Yet, to get a quantitative agreement between the theory predictions and the measured speeds of tension propagation, the previous models used orders of magnitude lower values of the stretching modulus, such as $40 \text{ pN}/\mu\text{m}$ ^{1,5} and $100 \text{ pN}/\mu\text{m}$ ⁴. The former value originated from the measurements of the elastic deformations of neutrophils and characterized the stretching rigidity of the cytoskeletal networks of these cells rather than that of the cell membranes, as was explicitly stated in the original articles^{53,54}. The latter value was taken from⁸, where it was attributed to the membrane tension rather than the stretching modulus. This means that the membranes have been considered extremely soft as compared to the real cell membranes and lipid bilayers. If the quantitative estimations of^{4,5} used the proper values of the stretching modulus^{7,55}, the predicted speeds would exceed the experimentally observed values by at least three orders of magnitude. In this context, it is important to emphasize a potentially confusing issue of membrane rigidity for stretching. Two notions of stretching rigidity have been introduced to describe the elastic behavior of membranes. One is the

local rigidity, which sets a relationship between the membrane tension and the local changes of the in-plane density of the membrane material or, equivalently, the in-plane area stretching of the membrane⁷. The second is the effective stretching rigidity of the entropic origin, which relates the tension in an undulating membrane to the projection of the membrane area on the base plane⁵⁶. The two rigidity types drastically differ in both the underlying physics and the numerical values. While, as mentioned above, the local rigidity determines the relationship between the local stretching strains and stresses of the membrane material⁷, the effective stretching rigidity is set by, generally, weak resistance to smoothening of the membrane thermal undulations⁵⁶ and is, therefore, orders of magnitude smaller than the local stretching rigidity⁵⁵. It is essential to stress that the previously proposed mechanisms of the tension propagation were explicitly based on the local rather than the effective stretching rigidity since the membrane density fluctuations are generated within and propagate along the actual membrane plane even if the latter is dynamically wrinkled by undulations.

Here we proposed a mechanism of tension propagation, which naturally explains the whole spectrum of the observations based on the realistic values of the system parameters and, specifically, under an assumption of the membrane non-stretchability. The chief premise of the model is a subdivision of the membrane into about 200 nm large compartments by fences consisting of trans-membrane picket-proteins attached to the sub-membrane cortical cytoskeleton³², and the membrane buckling within each compartment by the contractile cortical layer leading to generation of an excess membrane area. Extending the original idea of the picket-fence model, according to which the compartment boundaries restrict the in-plane diffusion of lipids and proteins^{32,39,40}, we assumed that they also serve as barriers for the in-plane flow of the membrane material.

The essence of the mechanism is that the positive membrane tension is produced in each compartment by the intracellular pressure so that the tension value depends on the pressure and the membrane excess area. The model predicts that an abrupt change of the excess area within a certain compartment by, for example, pulling out a membrane tether or through budding an endocytic vesicle⁵⁷, leads to an increase of the pressure-induced tension within this compartment. This generates tension differences between the perturbed and the surrounding compartments, which, in turn, induces an inter-compartment membrane flow to compensate for the loss of the local membrane area and the related tension perturbation. The rate of this flow, which depends on the intracellular pressure and the permeability of the compartment boundaries, sets the propagation speed of the tension perturbation along the system. The flow ceases when the tension is equalized along the membrane.

We provided experimental support to the model predictions by measuring the tension propagation in live cells exposed to hypotonic media. For this purpose, we modified the previously developed dual-tether pulling assay¹ such that the pulled tethers were mutually perpendicular, which eliminated the artifacts related to a possible movement of the whole cell. Our experiments demonstrated that cell exposure to hypotonic medium changes the tension propagation from nearly vanishing in isotonic conditions to, practically, instantaneous upon the transmembrane osmotic difference of about 75 mM or more. Provided that the application of a hypotonic medium changes the intracellular pressure and the membrane area excess⁴⁸, these results support the model predictions.

The limitation of our experiments was in measuring either, practically, vanishing or very large rates of tension propagation. We could not achieve the conditions of intermediate rates corresponding to the experimentally measurable propagation times in the range between ten seconds to a few minutes. The reason is that, according to the estimation based on (Eq. 3) the change of the propagation rate in the relevant range between $1\mu\text{m}/\text{min}$ and $10\mu\text{m}/\text{s}$ corresponds to a

variation of the trans-membrane difference of the osmotic concentration of about 1 mM, which is well beyond the experimental accuracy.

Importantly, besides the intracellular pressure, the predicted propagation speed of the tension perturbation substantially depends on a few other system parameters, such as the excess area within the membrane compartments, β_0 , the permeability of the compartment boundaries, λ , and the compartment size, a (Eq. 3). Therefore, an independent way to verify the model predictions would be to change the compartment size, a , and, hence, the inter-compartment excess area, β_0 , by modulating the contractility of myosin II in the cortical cytoskeleton. We attempted to perform this verification of the model by affecting the activity of myosin II by either treating the cells with Blebbistatin to inhibit myosin II activity or by expressing Rho A to enhance myosin II activity (see SI E). Unfortunately, the results of these experiments presented in (Supplementary Fig. E1) were inconclusive. The reason for this is that changes in the myosin contractility have two mutually opposing effects. On one hand, a decrease in the myosin contractility is expected to weaken the membrane crumpling and, hence, reduce, β_0 , and increase a which according to (Eq. 3) must accelerate the tension propagation. On the other hand, it must decrease the intracellular pressure⁴¹, which, according to (Eq. 3) slows down the tension propagation. The analogous reasoning is true for the increase of the myosin II contractility. Which of the two counteracting effects dominates, may depend on the system and specific conditions. In our system they are, obviously, mutually compensated.

While the parameters a , β_0 , and λ , can vary between different cell types and intracellular conditions, the few orders of magnitude large range observed for variations of the tension propagation rate can be feasibly explained only by the difference in intracellular pressure, P , shown to vary in the range between tens of Pa and several kPa⁴², and possibly by the variations in the excess area created by the cortical cytoskeleton.

To support the adequacy of our model, we checked its ability to recover the results of our measurements. For this purpose, we numerically solved the diffusion-like equation of the tension propagation in realistic conditions of a spherical membrane subjected to a continuous rather than instantaneous pulling of a membrane tether (SI F). This allowed us to computationally reproduce the time evolution of the pulling forces acting on the two tethers (SI F) and compare it with the results of a representing experiment (SI G). This analysis described in detail in (SI F,G) demonstrated a good agreement between the theory predictions and the results of our measurements (Supplementary Fig. G1) for the reasonable parameter values, hence, substantiating our model.

It must be emphasized that the theoretical analysis of the proposed model includes simplifications. One simplifying assumption was about the smallness of the perturbation of the compartment area excess. In reality, this assumption may be violated to some extent. Therefore, the present results must be seen as semi-quantitative. Additional factors neglected by our model are the possible deviations of the compartment boundaries from the circular shape and variations of the compartment sizes. While, according to our estimations, these factors do not qualitatively change the model predictions, the evaluation of the related effects requires numerical simulations, which are beyond the scope of the present work. Further, in our proof-of-principle estimations of the changes in the effective diffusion coefficient, D , upon cell exposure to hypotonic mediums, we assumed all the parameters determining D , except, for the pressure, P , to remain constant. The approximate constancy of the compartment radius, a , has been confirmed by the experiments (Fig. 5 and Supplementary Figs. D7, D8). This also means the permeability of the compartment boundaries, λ , and the excess area, β_0 , should not substantially change. Indeed, λ , is set by the linear density of the picket-proteins along the compartment boundary (see SI B). Since, upon constant a , the

boundaries do not change their length the linear picket protein density and, hence, the permeability λ must remain nearly constant. Also the excess area, β_0 , would vary if the compartment base area changed, which does not happen provided that α remains constant.

Finally, the physics principle of the proposed model may have a general character and underly the slowing down of the tension propagation also by membrane bulges and protrusions representing membrane superstructures such as caveolae⁵⁸ and microvilli⁵³ shaped by specialized protein complexes and machineries. Such membrane superstructures can accumulate much more membrane area^{48,53,54,59–61} than the amount of about 10% generated by the cortex contraction as we estimated based on the data⁴¹. The essence of the suggested concept is the existence of an inverse dependence of the membrane tension on the excess area accumulated in the membrane compartment. The tension must increase with a decrease in the excess area. In the specific model considered here, this dependence is established through the Laplace-like relationship between the tension, the intracellular pressure, and the excess area. In case the excess area is stored within the protein-dependent membrane bulges, the tension propagation will be slowed if a continuous smoothening of a bulge is related to an increase of the tension. The specific relationship between the extent of the bulge smoothening and the tension would determine the rate of the tension propagation. Currently, no data is available on such relationships either for caveolae or microvilli or any other familiar membrane super-structures. Yet, this is an exciting subject for future studies.

Methods

Cell culture

HEK293T (ATCC CRL-3216TM) cells were cultured at 37 °C and 5% CO₂ in DMEM (Gibco-Thermo Fisher scientific 11995065) supplemented with 10% Fetal bovine serum (biological industries, 04-001-1 A) and 1% penicillin-streptomycin (Gibco-Thermo Fisher scientific 15140122).

Orthogonal dual-tether pulling from cells assay

The experiments were performed using a C-trap® confocal fluorescence optical tweezers setup (LUMICKS, Amsterdam, the Netherlands) made of an inverted microscope based on a water-immersion objective (NA 1.2) together with a condenser top lens placed above the flow cell. The optical traps are generated by splitting a 10 W 1064-nm laser into two orthogonally polarized, independently steerable optical traps. To steer the two traps, one coarse-positioning piezo stepper mirror and one accurate piezo mirror were used. Optical traps were used to capture polystyrene microbeads. The displacement of the trapped beads from the center of the trap was measured and converted into a force signal by back-focal plane interferometry of the condenser lens using two position-sensitive detectors. The samples were illuminated by a bright field 850-nm LED and imaged in transmission onto a metal-oxide-semiconductor (CMOS) camera. **Confocal fluorescence microscopy:** The C-Trap uses a 3 color, fiber-coupled laser with wavelengths 488, 561 and 638 nm for fluorescence excitation. Scanning was done using a fast tip/tilt piezo mirror. For confocal detection, the emitted fluorescence was descanned, separated from the excitation by a dichroic mirror, and filtered using an emission filters (Blue: 500–550 nm, Green: 575–625 nm and Red: 650–750 nm). Photons were counted using fiber-coupled single-photon counting modules. The multimode fibers serve as pinholes providing background rejection. For confocal imaging the 532 nm laser was used for DiI-C12 excitation with 5% laser power, 54.34 μ W is the maximal laser power, and the emission detected in the green channel. **Sample preparation: Bottom glass dish setup:** 16–20 h before the experiment HEK293T cells were plated, at 20% confluency in 35 mm glass bottom dish (Bar Naor BN200350NW) coated with poly-L-lysine (Sigma-Aldrich P6282). 15 minutes before the experiment the cells were stained with 2 μ g/ml DiI-C12 (Invitrogen) membrane dye, washed with HEPES buffer (20 mM

HEPES, 150 mM NaCl, 2 mM CaCl₂, pH 7.4) twice, and then incubated in HEPES buffer with different NaCl concentrations as indicated in the text (0, 50, 75, 100 or 150 mM). **Flow-cell setup:** HEK293T cells were stained with 2 μ g/ml DiI-C12 (Invitrogen) membrane dye for 15 min, washed with PBS buffer, harvested with trypsin, centrifuged and resuspended in DMEM media. Next, the cells were injected at 0.1 bar (or lower pressure) into a 5 channels laminar flow cell (u-Flux, LUMICKS, Amsterdam, the Netherlands), which had been precoated with poly-L-lysine (Sigma-Aldrich P6282). After the cells settled at the bottom of the flow cell, HEPES buffer with the desired NaCl concentration was injected to flow cell. **Tether pulling:** The sample was mounted onto the automated XY-stage of the C-trap and 3.43 μ m polystyrene beads (Spherotech) or 1.88 μ m polystyrene beads (Spherotech) were added to the sample. A membrane tube was pulled from a cell using an optically trapped bead (bead 1). The tether was pulled by moving the trapped bead towards the cell until it touched the cell. The contact between the bead and the cell was verified by the trapping force (which is calculated from the displacement of the bead from the laser beam). The first tether was pulled in the X axis or in the Y axis of the C-trap, i.e., the pulling force of the tether had only one component, X or Y. Next, a second tether was pulled from the cell, using a second trapped bead (bead 2) in a direction which is perpendicular to the first tether (unless mentioned otherwise). After pulling the orthogonal tethers, we oscillated bead 1 in the same direction in which the tether was pulled, and monitored the response of the second bead in both axis (X, Y). The response was monitored using the trapping force of the second trap and/or using the subpixel particle tracking of the video analysis in BlueLake software. The response of the second bead should be only in the perpendicular direction of the movement of the first bead. If there was a response in the parallel direction, the measurement was not taken into account. At the end of each measurement the traps were shut down in order to ensure that the tethers were immediately pulled back towards the cells (Supplementary Movie 5). Data where tethers were not retracted as in (Supplementary Movie 6) were excluded.

Orthogonal dual-tether pulling from cells with single extension of tether 1 assay

The experiments were performed as described in the orthogonal dual-tether pulling from cells assay section in the flow-cell setup. However, in these experiments, after pulling the orthogonal tethers, we did not oscillate bead 1. Instead, we extended tether 1 by moving bead 1 in the same direction the tether was pulled, and monitored the response of bead 2.

Orthogonal dual-tether pulling from cells with RhoA

HEK293T cells at 50% confluency were transiently transfected with 5 μ g pcDNA3-EGFP-RhoA-Q63L (Addgene) using Lipofectamine 2000 (Invitrogen, Thermo Fisher scientific) according to the manufacture's protocols, and then grown for 24 h. Following the protein expression, the cells were stained with 2 μ g/ml DiI-C12 (Invitrogen) membrane dye for 15 min, washed with PBS buffer, harvested with trypsin, centrifuged and resuspended in DMEM media. Next, the cells were injected at 0.1 bar (or lower pressure) into a 5 channels laminar flow cell (u-Flux, LUMICKS, Amsterdam, the Netherlands), which had been precoated with poly-L-lysine (Sigma-Aldrich P6282). After the cells settled at the bottom of the flow cell, HEPES buffer with 50 mM NaCl was injected into the flow cell.

Orthogonal dual-tether pulling from cells incubated with blebbistatin

HEK293T cells were incubated with 100 or 200 μ M Blebbistatin. Following the incubation, the cells were stained with 2 μ g/ml DiI-C12 (Invitrogen) membrane dye for 15 min, washed with PBS buffer, harvested with trypsin, centrifuged and resuspended in DMEM media.

Next, the cells were injected at 0.1 bar (or lower pressure) into a 5 channels laminar flow cell (u-Flux, LUMICKS, Amsterdam, the Netherlands), which had been precoated with poly-L-lysine (Sigma-Aldrich P6282). After the cells settled at the bottom of the flow cell, HEPES buffer with 100 mM NaCl with 100 or 200 μ M Blebbistatin was injected to the flow cell.

Tether pulling force

16–20 h before the experiment HEK293T cells were plated, at 20% confluency in 35 mm glass bottom dish (Bar Naor BN200350NW) coated with poly-L-lysine (Sigma-Aldrich P6282). Before the experiment, the cells were stained with 2 μ g/ml DiI-C12 (Invitrogen) membrane dye for 15 minutes, washed with HEPES buffer twice, and then incubated in HEPES buffer with different NaCl concentrations as indicated in the text (50 and 150 mM). The sample was mounted onto the automated XY-stage of the C-trap and 1.88 μ m polystyrene beads (SpheroTech) were added to the sample. Using an optically trapped bead, a membrane tube with a length of 6.5 μ m was pulled from a cell for measuring the tether-pulling force.

Cell volume measurement

16–20 h before the experiment HEK293T cells were plated, at 20% confluency in 35 mm glass bottom dish (Bar Naor BN200350NW) coated with poly-L-lysine (Sigma-Aldrich P6282). Before the experiment, the cells were stained with 2 μ g/ml DiI-C12 (Invitrogen) membrane dye for 15 minutes, washed with HEPES buffer twice, and then incubated in HEPES buffer with different NaCl concentrations as indicated in the text (50 and 150 mM). The sample was imaged with Zeiss LSM 880 confocal microscope using 40 \times water immersion and 10 \times objective lenses (Zeiss) with a 30-mW argon laser (514 nm). Confocal slices were acquired with a 2 μ m step in the z-direction. The volume individual cells was measured from the 3D images using the Imaris software. The surface analysis tool was used to calculate the cell volume.

Sliding tether assay

16–20 h before the experiment HEK293T cells were plated, at 20% confluency in 35 mm glass bottom dish (Bar Naor BN200350NW) coated with poly-L-lysine (Sigma-Aldrich P6282). Before the experiment, the cells were stained with 2 μ g/ml DiI-C12 (Invitrogen) membrane dye for 15 minutes, washed with HEPES buffer twice, and then incubated in HEPES buffer with different NaCl concentrations as indicated in the text (0, 50 and 150 mM). The sample was mounted onto the automated XY-stage of the C-trap and 3.43 μ m polystyrene beads (SpheroTech) were added to the sample. A membrane tube was pulled from a cell using an optically trapped bead. The tether was then extended sideways by moving the bead.

Single particle tracking of EGFR in cells

HEK293T cells were grown in Dulbecco's Modified Eagle Medium supplemented with 10% fetal bovine serum (FBS), 2 mM glutamine, 10 000 U ml⁻¹ penicillin, and 10 mg ml⁻¹ streptomycin. For imaging, cells were plated 24 h before transfection at 30% confluency on an Ibidi Glass Bottom Dish 35 mm (Martinsried, Germany). Cells were subjected for Genetic Code expansion (GCE) as described in König et al.⁶². In short, cells were transfected using Lipofectamine 2000 (Life Technologies, Carlsbad, CA) with a plasmid construct encoding a Pyrrolysine tRNA synthetase (PylRS) that aminoacylates BCNK, a single orthogonal amber suppressor tRNA^{CUA}, and an EGFR with an in-frame stop codon at position 128. Transfected cells were incubated for 24 h in the presence of BCNK (0.5 mM; Synaffix, Oss, Netherlands) and washed with fresh medium at 37 °C. Labeling was then carried out in the dark (30 min 37 °C) with 1.5 μ M of the non-cell permeable dye, Tet-Cy3 (Jena Bioscience GmbH, Jena, Germany)⁶³. Finally, cells were washed and imaged in a HEPES buffer containing different salt concentrations (0,

50 or 150 mM NaCl), as indicated. Cells were kept at 4 °C until imaged to avoid EGFR internalization. Cells were then subjected to imaging on the Zeiss Elyra inverted wide field fluorescence microscope using a Zeiss 100X N.A 1.46 TIRF oil immersion objective in HiLo mode, focusing on the bottom of the cells. Excitation was achieved using solid-state lasers (561 nm for Tet-Cy3). Movie series were recorded on an electron-multiplying charge-coupled device camera (iXon DU897, Andor, Belfast, Northern Ireland) at a frame rate of 20 fps for 1 minute.

Videos were analyzed using the Trackpy⁶⁴ python implementation of the Crocker Grier⁶⁵ algorithm. Detected proteins were filtered by size, signal, and eccentricity to eliminate spurious instances not representing membranous single-molecule diffusion, such as protein aggregates, proteins located at cell edges, and fluorophores detected outside cells.

Protein diffusion was characterized by calculating the time-averaged Mean Squared Displacement (MSD) of each particle,

$$\text{MSD}(\tau) = \frac{1}{T - \tau} \sum_{t=0}^{T-\tau} (r(t + \tau) - r(t))^2,$$

where τ is the lag time, T is the total length of the trajectory, and $r(t)$ is the location of the protein at time t . To account for bias resulting from insufficient statistics in short trajectories, only trajectories longer than 30 frames were used in these calculations. Following that, an ensemble and time average MSD for each condition was calculated by averaging all time-average MSDs within that condition.

Giant plasma membrane vesicle (GPMVs) formation

GPMVs were produced according to a published protocol⁶⁶. Briefly, HEK293T cells were stained with DiI-C12 (Invitrogen) membrane dye, washed with GPMV buffer (20 mM HEPES, 150 mM NaCl, 2 mM CaCl₂, pH 7.4) twice, and incubated with 1 mL of GPMV buffer containing 1.9 mM DTT (Sigma) and 27.6 mM formaldehyde (Sigma). Secreted GPMVs were then collected and isolated from the cells and immediately used for the experiments.

Fluorescence recovery after photobleaching

Fluorescence recovery after photobleaching (FRAP) was carried out using a Leica SP8 TCS confocal microscope (Leica Microsystems, Wetzlar, Germany). The cells were imaged with a 63X1.4 NA objective using FRAP settings of λ_{ex} = 561 nm laser excitation wavelength and λ_{em} = 575–680 emission wavelength range. 5 iteration scans were performed before bleaching using 20% of the 561 nm laser. A rectangular region of interest (10 \times 1 μ m) was bleached by a short laser pulse (30 iterations of 100% 561 nm laser), and the fluorescence recovery was monitored for 35 seconds (80 iterations of 20% 561 nm laser) against a reference region of interest within the same membrane area. For FRAP experiments conducted on GPMVs the bleached area was (5 \times 1 μ m) due to their smaller size compared to cells. To compensate for the smaller bleaching area in the FRAP experiments of GPMVs, the recovery half time of each measurement in the GPMVs experiments was multiplied by a factor of 2. In practice, this factor should be lower than 2 because the bleached area of the GPMVs is curved (part of a sphere) and therefore the length of the bleached curve is higher than 5 μ m. The images and the fluorescence intensity profile were exported using Leica software.

Data analysis

Data acquisition for the dual-tether pulling assay was carried out using Bluelake, a commercial software from Lumicks. This software stores experimental data acquired with the C-trap in HDF5 files, which can be processed using Lumicks' Pylake python package. Images of the confocal scans were reconstituted from photon count per pixel data in the HDF5 files using Pylake. All data analysis was performed with custom-written Python scripts.

The force measured by C-trap is sampling 79,000 data points per second. Since our experiments are quite long, we downsized the force data to 79 data points per second for convenient presentation.

For FRAP analysis we used EasyFrap software⁶⁷ to normalize the FRAP data and to obtain the half time of the maximal fluorescence recovery.

Statistics and Reproducibility

No statistical method was used to predetermine sample size. The Investigators were not blinded to allocation during experiments and outcome assessment.

Reporting summary

Further information on research design is available in the Nature Portfolio Reporting Summary linked to this article.

Data availability

The raw data for Pearson correlation analysis in Fig. 3, FRAP measurements in Supplementary Fig. D7, single-particle tracking in Supplementary Fig. D8, the force amplitude of tether2 in Supplementary Fig. D6, and the plasmid map of RhoA were deposited in the OSF repository [<https://osf.io/t7vmf/>]. All other data supporting the findings of this study are available in this article, its supplementary information, or the Source Data file. Source data are provided with this paper.

Code availability

Computer code used for data analysis is available on GitLab [<https://gitlab.com/sorkin.raya/tension-propagation-project>].

References

- Shi, Z., Graber, Z. T., Baumgart, T., Stone, H. A. & Cohen, A. E. *Cell Membr. Resist Flow. Cell* **175**, 1769–1779 e1713 (2018).
- Shi, Z., Innes-Gold, S. & Cohen, A. E. Membrane tension propagation couples axon growth and collateral branching. *Sci. Adv.* **8**, eabo1297 (2022).
- Gomis Perez, C. et al. Rapid propagation of membrane tension at retinal bipolar neuron presynaptic terminals. *Sci. Adv.* **8**, eabl4411 (2022).
- De Belly, H. et al. Cell protrusions and contractions generate long-range membrane tension propagation. *Cell* **186**, 3049–3061 e3015 (2023).
- Cohen, A. E. & Shi, Z. Do Cell Membranes Flow Like Honey or Jiggle Like Jello? *Bioessays* **42**, e1900142 (2020).
- Helfrich, W. Elastic Properties of Lipid Bilayers - Theory and Possible Experiments. *Z. Naturforsch. C. C.* **28**, 693–703 (1973).
- Evans, E. & Skalak, R. *Mechanics and Thermodynamics of Biomembranes*. (CRC Boca Raton, Florida; 1980).
- Sens, P. & Plastino, J. Membrane tension and cytoskeleton organization in cell motility. *J. Phys. Condens Matter* **27**, 273103 (2015).
- Kozlov, M. M. & Mogilner, A. Model of polarization and bistability of cell fragments. *Biophys. J.* **93**, 3811–3819 (2007).
- Sitarska, E. & Diz-Munoz, A. Pay attention to membrane tension: Mechanobiology of the cell surface. *Curr. Opin. Cell Biol.* **66**, 11–18 (2020).
- Pontes, B., Monzo, P. & Gauthier, N. C. Membrane tension: A challenging but universal physical parameter in cell biology. *Semin Cell Dev. Biol.* **71**, 30–41 (2017).
- Keren, K. et al. Mechanism of shape determination in motile cells. *Nature* **453**, 475–480 (2008).
- Hetmanski, J. H. R. et al. Membrane Tension Orchestrates Rear Retraction in Matrix-Directed Cell Migration. *Dev. Cell* **51**, 460–475.e410 (2019).
- Houk, A. R. et al. Membrane tension maintains cell polarity by confining signals to the leading edge during neutrophil migration. *Cell* **148**, 175–188 (2012).
- Lieber, A. D., Schweitzer, Y., Kozlov, M. M. & Keren, K. Front-to-rear membrane tension gradient in rapidly moving cells. *Biophys. J.* **108**, 1599–1603 (2015).
- Lieber, A. D., Yehudai-Resheff, S., Barnhart, E. L., Theriot, J. A. & Keren, K. Membrane tension in rapidly moving cells is determined by cytoskeletal forces. *Curr. Biol.* **23**, 1409–1417 (2013).
- De Belly, H. et al. Membrane Tension Gates ERK-Mediated Regulation of Pluripotent Cell Fate. *Cell Stem Cell* **28**, 273–284.e276 (2021).
- Bergert, M. et al. Cell Surface Mechanics Gate Embryonic Stem Cell Differentiation. *Cell Stem Cell* **28**, 209–216.e204 (2021).
- Wu, X. S. et al. Membrane Tension Inhibits Rapid and Slow Endocytosis in Secretory Cells. *Biophys. J.* **113**, 2406–2414 (2017).
- Dai, J. & Sheetz, M. P. Regulation of endocytosis, exocytosis, and shape by membrane tension. *Cold Spring Harb. Symp. Quant. Biol.* **60**, 567–571 (1995).
- Masters, T. A., Pontes, B., Viasnoff, V., Li, Y. & Gauthier, N. C. Plasma membrane tension orchestrates membrane trafficking, cytoskeletal remodeling, and biochemical signaling during phagocytosis. *Proc. Natl Acad. Sci. USA* **110**, 11875–11880 (2013).
- Gauthier, N. C., Fardin, M. A., Roca-Cusachs, P. & Sheetz, M. P. Temporary increase in plasma membrane tension coordinates the activation of exocytosis and contraction during cell spreading. *Proc. Natl Acad. Sci. USA* **108**, 14467–14472 (2011).
- Keren, K. Cell motility: the integrating role of the plasma membrane. *Eur. Biophys. J.* **40**, 1013–1027 (2011).
- Saha, S., Nagy, T. L. & Weiner, O. D. Joining forces: crosstalk between biochemical signalling and physical forces orchestrates cellular polarity and dynamics. *Philos Trans R Soc Lond B Biol Sci* **373** (2018).
- Schweitzer, Y., Lieber, A. D., Keren, K. & Kozlov, M. M. Theoretical analysis of membrane tension in moving cells. *Biophys. J.* **106**, 84–92 (2014).
- Ofer, N., Mogilner, A. & Keren, K. Actin disassembly clock determines shape and speed of lamellipodial fragments. *Proc. Natl Acad. Sci. USA* **108**, 20394–20399 (2011).
- Mueller, J. et al. Load Adaptation of Lamellipodial Actin Networks. *Cell* **171**, 188–200 e116 (2017).
- Charras, G. & Paluch, E. Blebs lead the way: how to migrate without lamellipodia. *Nat. Rev. Mol. Cell Biol.* **9**, 730–736 (2008).
- Mussel, M. & Schneider, M. F. Sound pulses in lipid membranes and their potential function in biology. *Prog. Biophys. Mol. Bio* **162**, 101–110 (2021).
- Salbreux, G., Charras, G. & Paluch, E. Actin cortex mechanics and cellular morphogenesis. *Trends Cell Biol.* **22**, 536–545 (2012).
- Chugh, P. & Paluch, E. K. The actin cortex at a glance. *J. Cell Sci.* **131** (2018).
- Kusumi, A. et al. Paradigm shift of the plasma membrane concept from the two-dimensional continuum fluid to the partitioned fluid: high-speed single-molecule tracking of membrane molecules. *Annu Rev. Biophys. Biomol. Struct.* **34**, 351–378 (2005).
- Bussell, S. J., Koch, D. L. & Hammer, D. A. Effect of hydrodynamic interactions on the diffusion of integral membrane proteins: diffusion in plasma membranes. *Biophys. J.* **68**, 1836–1849 (1995).
- Bretscher, A., Edwards, K. & Fehon, R. G. ERM proteins and merlin: integrators at the cell cortex. *Nat. Rev. Mol. Cell Biol.* **3**, 586–599 (2002).
- Biro, M. et al. Cell cortex composition and homeostasis resolved by integrating proteomics and quantitative imaging. *Cytoskeleton (Hoboken)* **70**, 741–754 (2013).

36. Kusumi, A. et al. Dynamic organizing principles of the plasma membrane that regulate signal transduction: commemorating the fortieth anniversary of Singer and Nicolson's fluid-mosaic model. *Annu Rev. Cell Dev. Biol.* **28**, 215–250 (2012).
37. Kusumi, A., Suzuki, K. G., Kasai, R. S., Ritchie, K. & Fujiwara, T. K. Hierarchical mesoscale domain organization of the plasma membrane. *Trends Biochem Sci.* **36**, 604–615 (2011).
38. Jacobson, K., Liu, P. & Lagerholm, B. C. The Lateral Organization and Mobility of Plasma Membrane Components. *Cell* **177**, 806–819 (2019).
39. Fujiwara, T., Ritchie, K., Murakoshi, H., Jacobson, K. & Kusumi, A. Phospholipids undergo hop diffusion in compartmentalized cell membrane. *J. Cell Biol.* **157**, 1071–1081 (2002).
40. Fujiwara, T. K. et al. Confined diffusion of transmembrane proteins and lipids induced by the same actin meshwork lining the plasma membrane. *Mol. Biol. Cell* **27**, 1101–1119 (2016).
41. Stewart, M. P. et al. Hydrostatic pressure and the actomyosin cortex drive mitotic cell rounding. *Nature* **469**, 226–230 (2011).
42. Chengappa, P., Sao, K., Jones, T. M. & Petrie, R. J. Intracellular Pressure: A Driver of Cell Morphology and Movement. *Int Rev. Cell Mol. Biol.* **337**, 185–211 (2018).
43. Fischer-Friedrich, E., Hyman, A. A., Julicher, F., Muller, D. J. & Helenius, J. Quantification of surface tension and internal pressure generated by single mitotic cells. *Sci. Rep.* **4**, 6213 (2014).
44. Murase, K. et al. Ultrafine membrane compartments for molecular diffusion as revealed by single molecule techniques. *Biophys. J.* **86**, 4075–4093 (2004).
45. Cosson, P., Perrin, J. & Bonifacino, J. S. Anchors aweigh: protein localization and transport mediated by transmembrane domains. *Trends Cell Biol.* **23**, 511–517 (2013).
46. Miyagi, T. Viscous Flow at Low Reynolds Numbers past an Infinite Row of Equal Circular Cylinders. *J. Phys. Soc. Jpn.* **13**, 493–496 (1958).
47. Derenyi, I., Julicher, F. & Prost, J. Formation and interaction of membrane tubes (vol 88, art no 238101, 2002). *Phys. Rev. Lett.* **89** (2002).
48. Raucher, D. & Sheetz, M. P. Characteristics of a membrane reservoir buffering membrane tension. *Biophys. J.* **77**, 1992–2002 (1999).
49. Hsu, Y. Y., Irizarry, A. M. R., Fu, J. P. & Liu, A. P. Mechanosensitive Channel-Based Optical Membrane Tension Reporter. *Acs Sensors* (2023).
50. Roffay, C. et al. Passive coupling of membrane tension and cell volume during active response of cells to osmosis. *Proc. Natl. Acad. Sci. USA* **118** (2021).
51. Zucker, B. et al. Migrasome formation is initiated preferentially in tubular junctions by alternations of membrane tension or intracellular pressure. *bioRxiv*, 2023.2008.2003.551756 (2023).
52. Oppenheimer, N. & Diamant, H. In-plane dynamics of membranes with immobile inclusions. *Phys. Rev. Lett.* **107**, 258102 (2011).
53. Hochmuth, R. M. Micropipette aspiration of living cells. *J. Biomech.* **33**, 15–22 (2000).
54. Needham, D. & Hochmuth, R. M. A sensitive measure of surface stress in the resting neutrophil. *Biophys. J.* **61**, 1664–1670 (1992).
55. Evans, E. & Rawicz, W. Entropy-driven tension and bending elasticity in condensed-fluid membranes. *Phys. Rev. Lett.* **64**, 2094–2097 (1990).
56. Helfrich, W. & Servuss, R. M. Undulations, Steric Interaction and Cohesion of Fluid Membranes. *Nuovo Cim. D.* **3**, 137–151 (1984).
57. Marsh, M. & McMahon, H. T. The structural era of endocytosis. *Science* **285**, 215–220 (1999).
58. Sinha, B. et al. Cells respond to mechanical stress by rapid disassembly of caveolae. *Cell* **144**, 402–413 (2011).
59. Solsona, C., Innocenti, B. & Fernandez, J. M. Regulation of exocytotic fusion by cell inflation. *Biophys. J.* **74**, 1061–1073 (1998).
60. Groulx, N., Boudreault, F., Orlov, S. N. & Grygorczyk, R. Membrane reserves and hypotonic cell swelling. *J. Membr. Biol.* **214**, 43–56 (2006).
61. Figard, L. & Sokac, A. M. A membrane reservoir at the cell surface: unfolding the plasma membrane to fuel cell shape change. *Bioarchitecture* **4**, 39–46 (2014).
62. König, A. I. et al. Live cell single molecule tracking and localization microscopy of bioorthogonally labeled plasma membrane proteins. *Nanoscale* **12**, 3236–3248 (2020).
63. Uttamapinant, C. et al. Genetic code expansion enables live-cell and super-resolution imaging of site-specifically labeled cellular proteins. *J. Am. Chem. Soc.* **137**, 4602–4605 (2015).
64. Allan, B. et al. soft-matter/trackpy: Trackpy v0.5.0. Zenodo (2021).
65. Crocker, J. C. & Grier, D. G. Methods of Digital Video Microscopy for Colloidal Studies. *J. Colloid Interface Sci.* **179**, 298–231 (1996).
66. Gerstle, Z., Desai, R. & Veatch, S. L. Giant Plasma Membrane Vesicles: An Experimental Tool for Probing the Effects of Drugs and Other Conditions on Membrane Domain Stability. *Methods Enzymol.* **603**, 129–150 (2018).
67. Koulouras, G. et al. EasyFRAP-web: a web-based tool for the analysis of fluorescence recovery after photobleaching data. *Nucleic Acids Res* **46**, W467–W472 (2018).

Acknowledgements

We are grateful to Leonid Chernomordik, Haim Diamant, Naomi Oppenheimer, and Yael Roichman for helpful discussions and important suggestions. Michael Kozlov acknowledges support by the Israel Science Foundation (Grant No. 1994/22) and holds Joseph Klafter Chair in Biophysics. Raya Sorkin acknowledges support by the Israel Science Foundation (Grant No. 1289/20), and the NSF-BSF (Grant No. 2021793) and holds the Raymond and Beverly Sackler Career Development Chair for Young Faculty. Co-Funded by the European Union (ERC ReMembrane 101077502). Views and opinions expressed are however those of the authors only and do not necessarily reflect those of the European Union or the European Research Council Executive Agency. Neither the European Union nor the granting authority can be held responsible for them.

Author contributions

R.S. and R.D. conceived and planned the experimental studies. R.D., A.G., S.G., I.Y., D.N., N.E., R.S. performed/analyzed the experiments. A.B., A.K.T., M.M.K. conceived and performed the theoretical studies. R.S. and M.M.K. supervised the work.

Competing interests

The authors declare no competing interests.

Additional information

Supplementary information The online version contains supplementary material available at <https://doi.org/10.1038/s41467-024-55398-1>.

Correspondence and requests for materials should be addressed to Raya Sorkin or Michael M. Kozlov.

Peer review information *Nature Communications* thanks Bruno Goud, and the other, anonymous, reviewer(s) for their contribution to the peer review of this work. A peer review file is available.

Reprints and permissions information is available at <http://www.nature.com/reprints>

Publisher's note Springer Nature remains neutral with regard to jurisdictional claims in published maps and institutional affiliations.

Open Access This article is licensed under a Creative Commons Attribution-NonCommercial-NoDerivatives 4.0 International License, which permits any non-commercial use, sharing, distribution and reproduction in any medium or format, as long as you give appropriate credit to the original author(s) and the source, provide a link to the Creative Commons licence, and indicate if you modified the licensed material. You do not have permission under this licence to share adapted material derived from this article or parts of it. The images or other third party material in this article are included in the article's Creative Commons licence, unless indicated otherwise in a credit line to the material. If material is not included in the article's Creative Commons licence and your intended use is not permitted by statutory regulation or exceeds the permitted use, you will need to obtain permission directly from the copyright holder. To view a copy of this licence, visit <http://creativecommons.org/licenses/by-nc-nd/4.0/>.

© The Author(s) 2024